

Chapter I

1.1 Introduction

Finding the optimized surface for bone-implant interface is an important task in tissue engineering [1-4]. Many studies indicate that nanostructure such as nanofiber [5], sharp-tip [6], or nanotube affect cell proliferation [7]. Nanofiber could guide the dimension of cell proliferation. As the nanotopographical three-dimensionality of sharp-tip increased, the consistent trend of fewer cells and smaller cell size was observed. Cell adhesion and spreading were severely impaired on nanotube layers with a tube diameter larger than 50-nm, resulting in dramatically reduced cellular activity and a high extent of programmed cell death.

Surface topology encodes information that directs cell behavior. Cells detect and respond to specific ligands and spatial organization of the scaffoldings known as the extracellular matrix (ECM) [8-10]. Since ECM contains structures from micro-scale down to nano-scale, it is hypothesized that cells respond to both micro-structure and nano-structure [11-13].

Micro-scaled landscapes have been fabricated to direct growth of cultured cells [14]. When cultured on ridges and grooves of nanoscale dimensions, cells migrated more extensively to the ridges than into the grooves [15]. Cell shape was aligned and extended in the direction of the grooves. It has been shown that three-dimensional micro-structure that mimics ECM provides environment for in vivo growth of cells [16]. Osteoblasts grown on a fibrous matrix composed of multiwalled carbon nanofibers exhibited increased proliferation. Cells proliferate and form multicellular spheroids on interwoven polyamide fibers fabricated by electrospinning polymer solution onto glass slides [17]. Nanofibers have been fabricated to mimic the three-dimensional fibrous structure of the extracellular matrix [18]. 3-D nanofibrillar surfaces covalently modified with tenascin-C-derived peptides enhance neuronal

growth in vitro [19]. Although cellular response to microtopography has been intensively investigated, the nanotopography that cells respond to and molecular apparatus that sense and transmit spatial signal from membrane to nucleus are not clearly defined at the present time.

Nanotopography-induced cellular response has been explored using nanoislands [20]. Strong influence on the formation of focal adhesions, reorganization of cytoskeleton, and change in the mobility is observed. In our previous studies, we have shown differential growth of NIH-3T3 cells onto nanodot arrays with dot diameters ranging from 10-nm to 200-nm. Cells grew normally on the 10-nm array and on flat surfaces. However, 50-nm, 100-nm, and 200-nm nanodot arrays induced apoptotic events. The occurrence of apoptosis is mediated by the formation of focal adhesions. Application of assembly containing a range of nanostructures should be capable of obtaining parameters that are useful in the designing and evaluation of artificial implants in tissue engineering.

The current study is based on the hypothesis that nanotopography may modulate and control the growth, proliferation, and biological function of osteoblasts. Arrays of nanodots with defined diameter and depth can be fabricated by using aluminum nanopores as a template during oxidation of tantalum thin films. The dot size and the depth of dots are well controlled. It could serve as a convenient platform to optimize the bone-implant interface. Association of nanotopography with clinical outcome will be investigated and discussed.

1.2 Experimental Methods

1.2.1 Chemicals

Glutaraldehyde and osmium tetroxide were purchased from Electron Microscopy Sciences (USA). Anti-vinculin mouse antibody was purchased from Abcam (USA). Alexa Fluor 594 phalloidin, Alexa Fluor 488 goat anti-mouse IgG were purchased from Invitrogen (USA). Trypsin was purchased from Sigma (USA). Other chemicals of analytical grade or higher were purchased from Sigma or Merck.

1.2.2 Fabrication of nanodot arrays

Nanodot arrays were fabricated as described. Tantalum nitride (TaN) thin film of 200-nm in thickness was deposited onto a 6-inch silicon wafer followed by deposition of 400nm-thick aluminum on the top of a TaN layer. Anodization was carried out in 1.8 M sulfuric acid at 5 Volts for 10-nm nanodot array, in 0.3 M oxalic acid at 25 Volts, 100 Volts for 50-nm, and 100-nm nanodot arrays or in 5 % (w/v) phosphate acid (H_3PO_4) at 100 Volts for 200-nm nanodot arrays, respectively. Porous anodic alumina was formed during the anodic oxidation. The underlying TaN layer was oxidized into tantalum oxide nanodots using the alumina nanopores as template. The porous alumina was removed by immersing in 5 % (w/v) H_3PO_4 overnight. A thin layer of platinum (ca 5-nm) was sputtered onto the structure to improve biocompatibility. The dimension and homogeneity of nanodot arrays were measured and calculated from images taken by JEOL JSM-6500 TFE-Scanning electron microscopy (SEM).

1.2.3 Cell culture

MG63 cells were cultured in Dulbecco's Modified Eagle's Medium complimented with 10% FBS and 5% CO₂ and incubated at 37 °C.

1.2.4 Scanning electron microscopy

The harvested cells were fixed with 1% glutaraldehyde in phosphate buffered saline (PBS) at 4 °C for 20 minutes, followed by post-fixation in 1% osmium tetroxide for 30 minutes. Dehydration was performed through a series of ethanol concentrations (5 minutes incubation each in 50%, 60%, 70%, 80%, 90%, 95%, and 100% ethanol) and air dried. The specimen was sputter-coated with platinum and examined by JEOL JSM-6500 TFE-SEM at an accelerating voltage of 10 keV.

1.2.5 Immunostaining of vinculin and actin filament

Cells were harvested and fixed with 4% paraformaldehyde in PBS for 15 minutes followed by PBS wash for three times. Membrane was permeated by incubating in 0.1 % Triton X-100 for 10 minutes, followed by PBS wash for three times, blocked by 1 % bovine serum albumin (BSA) in PBS for 1 hour, and PBS wash for three times. The sample was incubated with anti-vinculin antibody (properly diluted in 0.5 % BSA) and phalloidin for 1 hour, followed by incubating with Alexa Fluor 488 goat anti-mouse antibody for 1 hour followed by PBS wash for three times.

1.2.6 Von Kossa staining

MG63 cells were harvested and fixed with 95% ethanol for 1 hour followed by DI-water wash for three times. Adding 5% silver nitrate solution and exposing to UV light for 20 minutes followed by DI-water wash for three times. The sample was added 5% thiosulphate

solution 5 minutes then washed for three times by DI-water. We randomly picked fifty cells for each condition and calculated the area of nodule per cell relative to the nodule per cell on flat surface.

1.2.7 Alizarin Red S staining

The MG63 cells on substrates were washed with PBS and fixed with 4% paraformaldehyde for 10 min. The fixed cells were soaked in 0.5% Alizarin Red S in PBS for 10 minutes at room temperature and washed with water to remove the remaining stains. We randomly picked fifty cells for each condition and calculated the area of stain per cell relative to the area of stain per cell on flat surface.



1.3 Results and Discussions

1.3.1 Fabrication of nanodot arrays for the growth of MG63

Nanodot arrays made by anodic aluminum oxide (AAO) template are highly packed and uniformly distributed in size and shape. It defines a series of nanotopology and can serve as an excellent model system to study how physical topography affects cellular behavior.

Nanodot arrays were fabricated as described previously by AAO processing on tantalum-coated wafer (Fig. 1a). Tantalum oxide nanodot arrays with dot diameters of 10-nm, 50-nm, 100-nm, and 200-nm were constructed on silicon wafer. To provide a biocompatible and unique interacting surface, platinum of ca 5-nm thickness was sputter-coated onto the top of the nanodot. Scanning electron microscopy (SEM) images showed diameters of 10 ± 2.8 nm, 52 ± 5.6 nm, 102 ± 9.2 nm, and 212 ± 18.6 nm for 10-nm, 50-nm, 100-nm, and 200-nm dot arrays, respectively (Fig. 1b). The average height was 11.3 ± 2.5 , 51.3 ± 5.5 , 101.1 ± 10.3 , and 154.2 ± 27.8 nm, respectively. Dimensions of nanodots were well-controlled and highly defined.

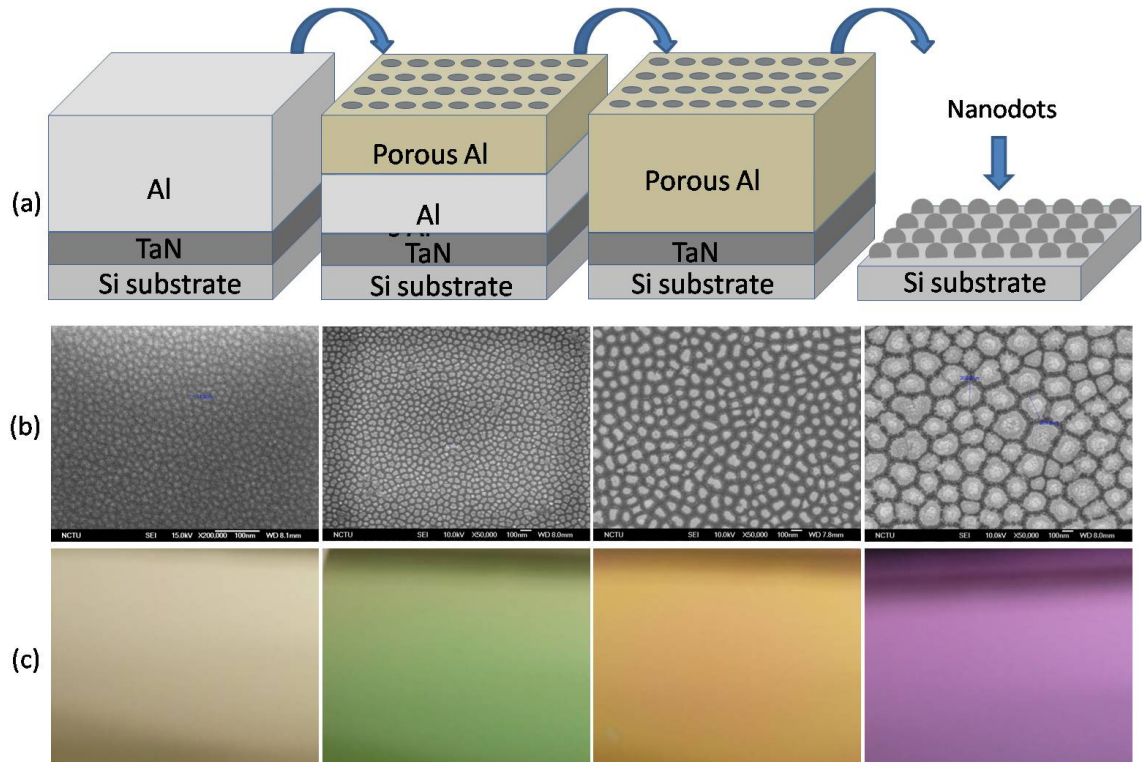


Fig. 1. Fabrication of tantalum-based nanodot arrays using AAO processing. (a) Schematic representation of fabrication of nanodot arrays. (b) SEM images of the fabricated nanodot arrays. (c) Photos of the fabricated nanodot arrays. Photos taken for the fabricated nanodot arrays exhibit different colors under visible light (from left to right): 10-nm nanodot array (10 nm), 50-nm nanodot array (50 nm), 100-nm nanodot array (100 nm), and 200-nm nanodot array (200 nm).

1.3.2 Nanostructure modulated proliferation, cell adhesion, and cytoskeleton organization of MG63

MG63 osteoblasts were cultured on fabricated nanodot arrays and on flat wafer at the density of 1,000 to 5,000 cells per square centimeter. Cells were harvested on day 3 after seeding. SEM was performed to examine the proliferation and morphology of cells (Fig. 2).

Cell density increased when the size of nanodots increased. However, the density reached a plateau at 50-nm but dropped dramatically for 100-nm and 200-nm nanodot arrays.

There are minor but visible differences in morphology for cells grown on different nanostructures. Morphology was flat and extended for cells grown on flat, 10-nm, and 50-nm nanodot arrays. In particular, cells grown on 50-nm nanodots exhibited much better morphology in the flatness and extended area. When the size increased to 100-nm, cells started to show thickening and mounting, especially at 200-nm. Best growth occurred to 50-nm nanodot arrays.

Number of focal adhesions is the hallmark for cell attachment and can be evaluated by the immunostaining against Vinculin (Fig. 2). Cells grown on the 50-nm nanodot exhibited the highest number of Vinculin staining compared to flat surface and 10-nm nanodots. Low levels of Vinculin staining were observed when the size increased to 100-nm and 200-nm. Best cell adhesion occurred to cells grown on 50-nm nanodot arrays.

Cytoskeleton organization indicated the growth state of cultured cells. Cells grown on flat, 10-nm, 50-nm, and 100-nm nanodots exhibited well defined actin filaments in the cytoplasm. However, there is a visible loss of actin filament for cells grown on 200-nm nanodots.

In general, cells grown on 50-nm nanodot arrays exhibited highest proliferation, flat and extended morphology, best cell adhesion, and well organized cytoskeleton.

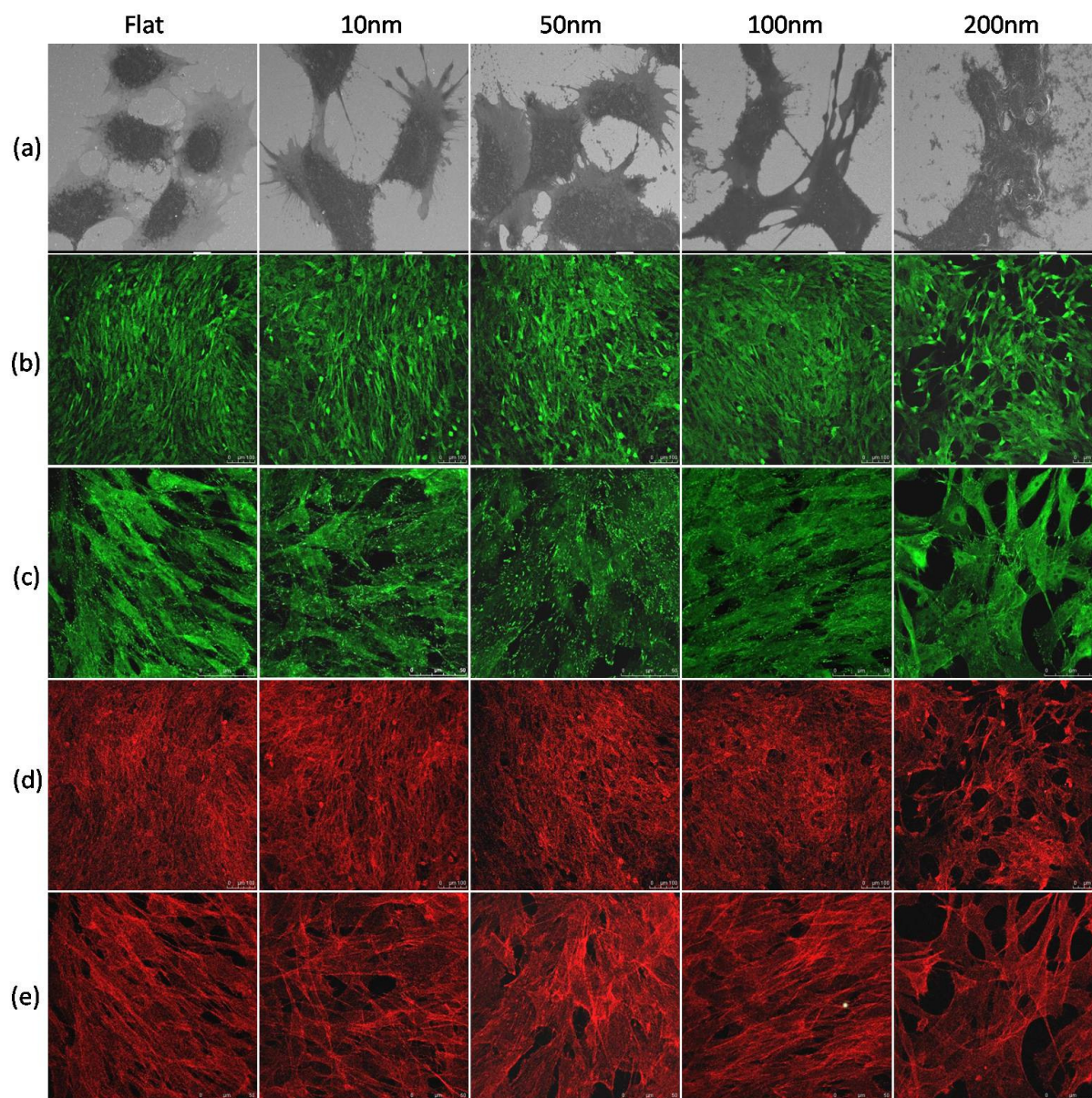


Fig. 2. Modulation for the growth, proliferation, and cytoskeleton of MG63. MG63 cells are cultured on nanodot arrays of dot size indicated on the top of images for 3 days. (a) SEM images of cells seeded on nanodot arrays. Immunostaining against Vinculin is performed to evaluate the formation of focal adhesions. The fluorescence images are taken at (b) 100X and (c) 400X. Immunostaining against actin filament is performed to visualize the organization of cytoskeleton. The fluorescence images are taken at (d) 100X and (e) 400X using confocal microscope. The sample was incubated with anti-vinculin antibody (properly diluted in 0.5 % BSA) and phalloidin, followed by incubating with Alexa Fluor 488 goat anti-mouse antibody.

1.3.3 Nanostructure modulated mineralization of MG63

Mineralization process is hallmark for osteobalsts. To investigate the modulation of mineralization process, MG63 cells were cultured onto various diameters of nanodot array for 7 days. Mineralization in cell culture monolayers has been determined by quantitative methods of the von Kossa staining and Alizarin Red S staining. Calcium phosphate was stained as dark crystals by von Kossa staining. The mineral was stained as bright red by Alizarin Red S staining. By von Kossa staining high density of nodular mineral deposit occurred to cells grown on 50-nm nanodots (Fig. 3 and 4). A 50% increase in mineral deposit compared to flat surface was found. Mineralization quantified by Alizarin Red S staining elicited 40% increase of mineral for cells grown on 50-nm nanodots (Fig. 5 and 6).

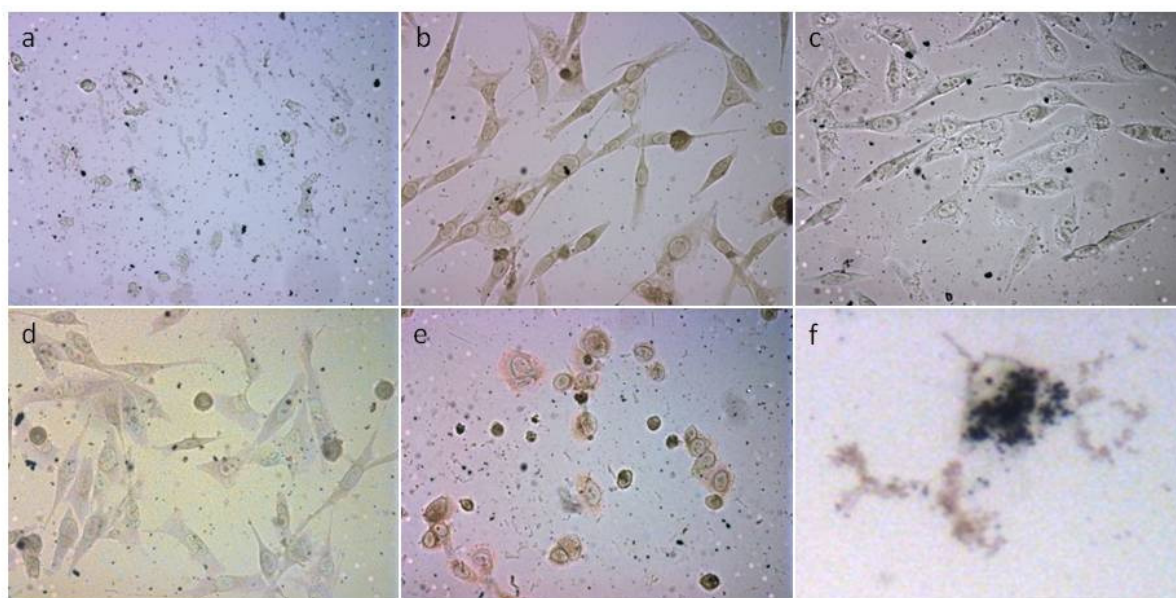


Fig. 3. Mineralization of cultured MG63 by the von Kossa staining process. MG63 cells are seeded onto nanodots and grow for 7 days. Mineralization of the cultured monolayer is assayed by the von Kossa staining process. Calcium phosphate was stained as dark crystals by von Kossa staining. Images are (a) cell grown on flat surface, (b) on 10-nm nanodots, (c) on 50-nm nanodots, (d) on 100-nm nanodots, (e) on 200-nm nanodots, and (f) enlarged image from (c).

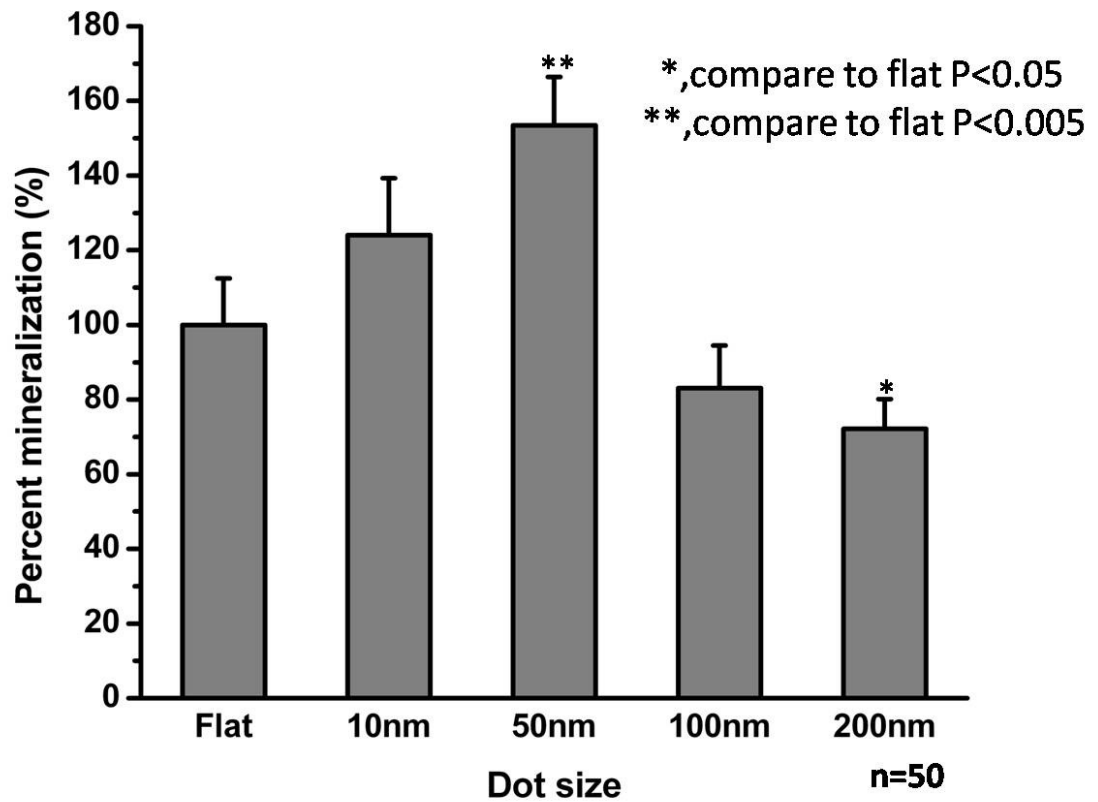


Fig. 4. Correlation between mineralization versus size of nanodot arrays. MG63 is cultured on various sizes of nanodot arrays for 7 days. The von Kossa staining procedure is performed. Percent mineralization is calculated using the area of dark crystal divided by the dark area for cells grown on flat surface. N equals to 50.

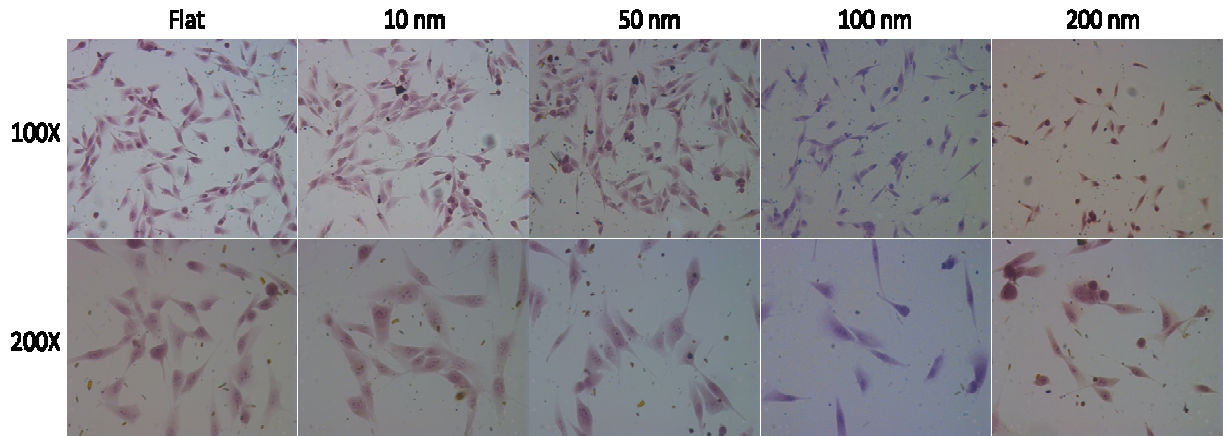


Fig. 5. Mineralization of cultured MG63 by Alizarin Red S staining. MG63 cells are seeded onto nanodots and grow for 7 days. The mineral was stained as bright red by Alizarin Red S staining. Sizes of nanodot array are indicated on the top of the images. Two sets of pictures are shown: 100X and 200X.

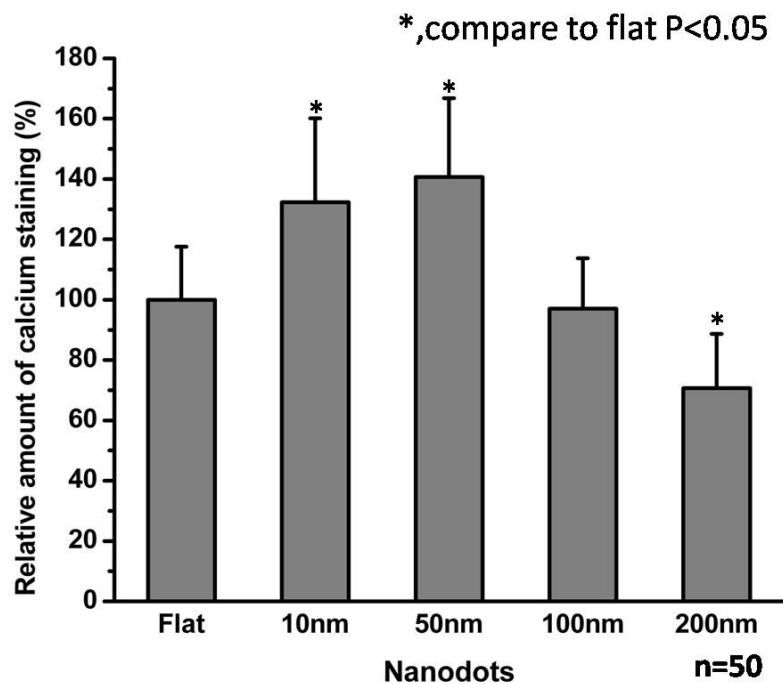


Fig. 6. Correlation between mineralization versus size of nanodot arrays. MG63 is cultured on various sizes of nanodot arrays for 7 days. The Alizarin Red S staining procedure is performed. Mineralization is calculated using the area of bright red. Relative mineralization is calculated relative to flat surface. N equals to 50.

1.3.4 Structural analysis for the clinical implants

The utility of nanostructure was further evaluated by the clinical test. Four kinds of commercially available implants were employed in the clinical tests, i.e. Uncoated, TPS, HA, and Nano Tite. Electron microscopy revealed the difference in microstructure and nanostructure (Fig. 7).

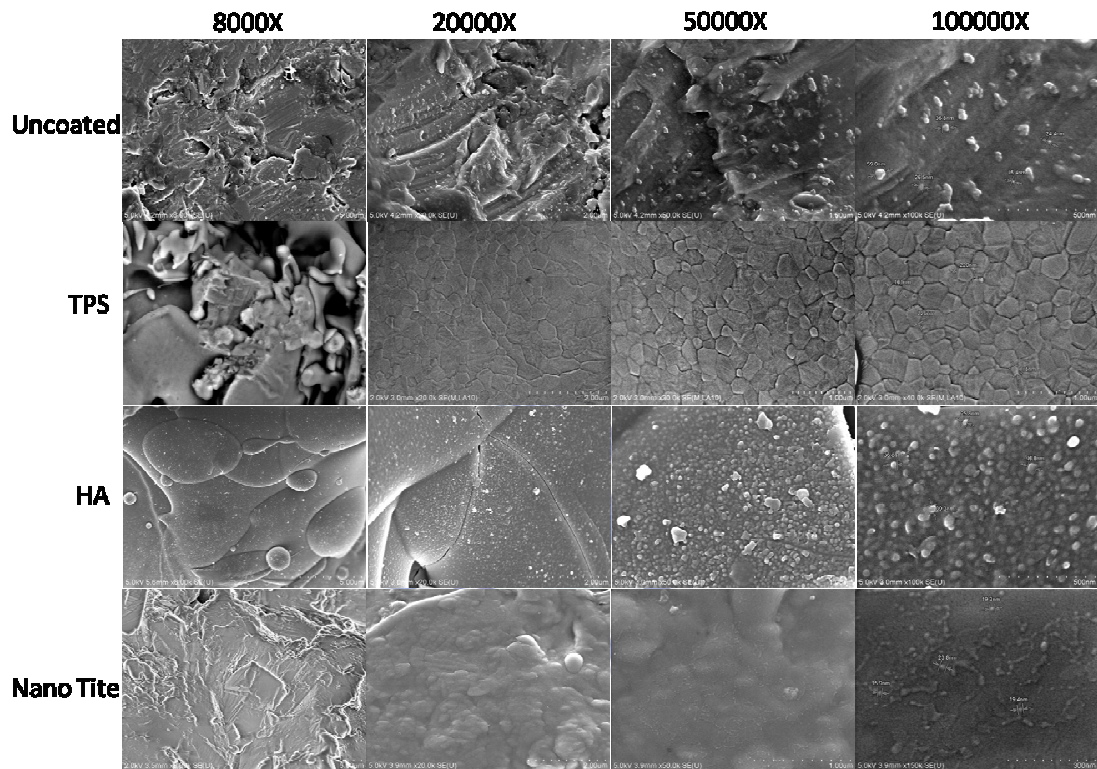



Fig. 7. SEM image showing the detail micro- and nano-structure of dental implants. There are 4 types of implants applied in the current clinical study: Uncoated, TPS, HA, and Nano Tite.

The Uncoated exhibited microscaled furrows of approximately 1 micron in height. There are also sparse particles-like nanostructure scattered on the surface with diverse diameters which averaged at approximately 50-nm. TPS contains hills and valleys at microscale which are unevenly scattered. There is no obvious nanostructure for TPS. However, nanoscale cracks were observed. HA contains less microstructure which exhibited as large hills of approximately 10 to 20 μm in diameter. HA also showed unexpectedly homogeneous distribution of nanoparticle-like structure distributed throughout the surface. The particles are homogeneous in size with averaged diameter of approximately 50-nm. Nano Tite contains microscale furrows less in number than Uncoated and with lower height. At also have much less nanostructure than other dental implants. The Dimension for the nanostructure on the surface of each type of implants was summarized in Table 1.

Table 1 Structural characterization for nanostructures on the dental implants



Type	Nanostructure size Average \pm SE (nm)
Uncoated	30.64 ± 18.17
TPS	181.25 ± 51.36
HA	41.98 ± 4.70
Nano Tite	19.6 ± 3.24

1.3.5 Evaluation of MG63 proliferation and growth on clinical implants

MG63 osteoblasts were grown onto 4 types of dental implants for 7 days. Number of cells grown on the implants was evaluated by DAPI staining for nuclei and actin fiber staining for cytoplasm (Fig. 8). MG63 was highly populated on Nano Tite and Uncoated, less populated on TPS, and dropped to much lower levels on HA.

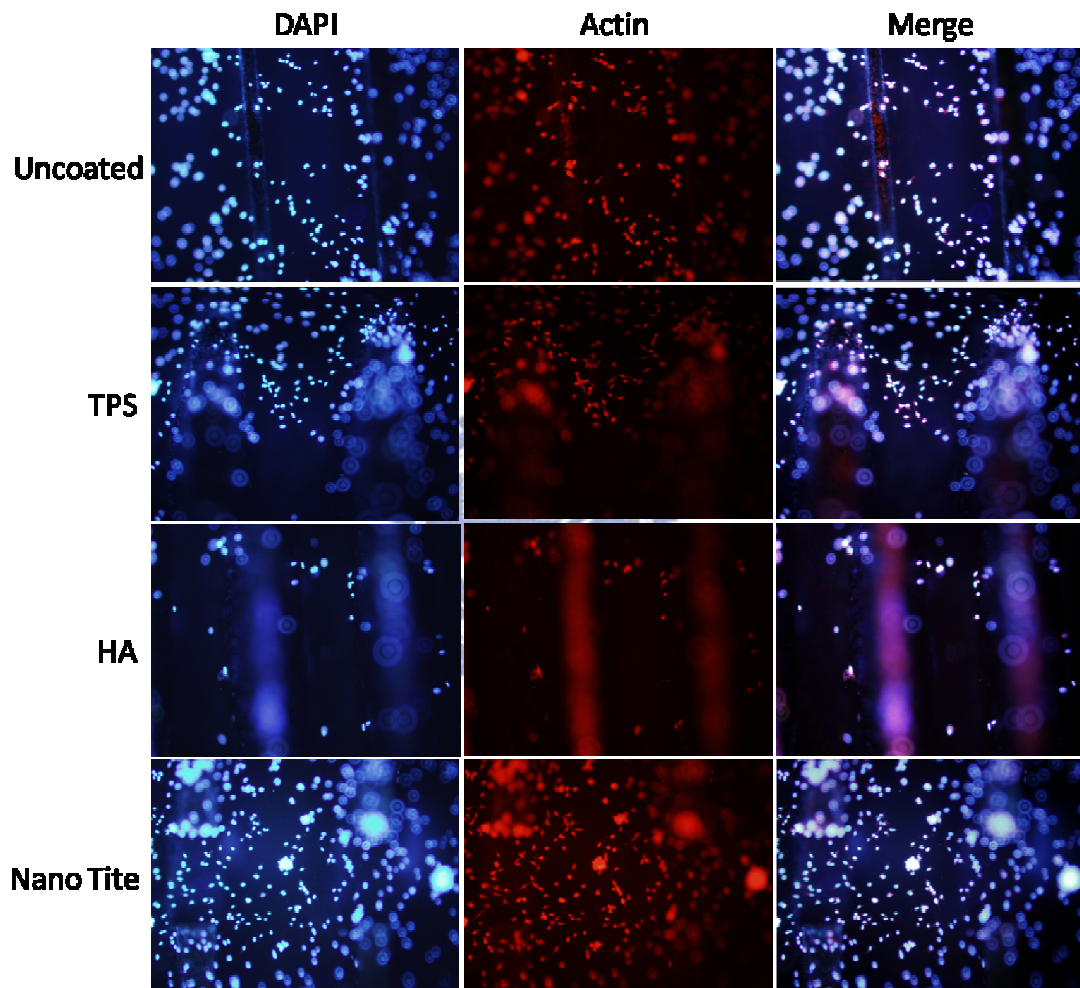


Fig. 8 Growth of MG63 onto implants. Cells are grown onto implants for 7 days and harvest. Nuclei are stained by DAPI. Cytoskeletons are visualized by immunostaining using antibody against actin filament. Images of DAPI staining and cytoskeleton staining are merged to show viable cells.

MG63 thus grown was also examined by SEM to observe the cell morphology (Fig. 9). MG63 was flat and extended when grown on HA, normal on TPS, started to exhibit apoptosis-like morphology on the Uncoated, and worst on Nano Tite. In summary, although population on implants indicated that the Uncoated and Nano Tite outgrow TPS and HA, the morphology indicated that HA and TPS are much suitable to grow MG63 on them.

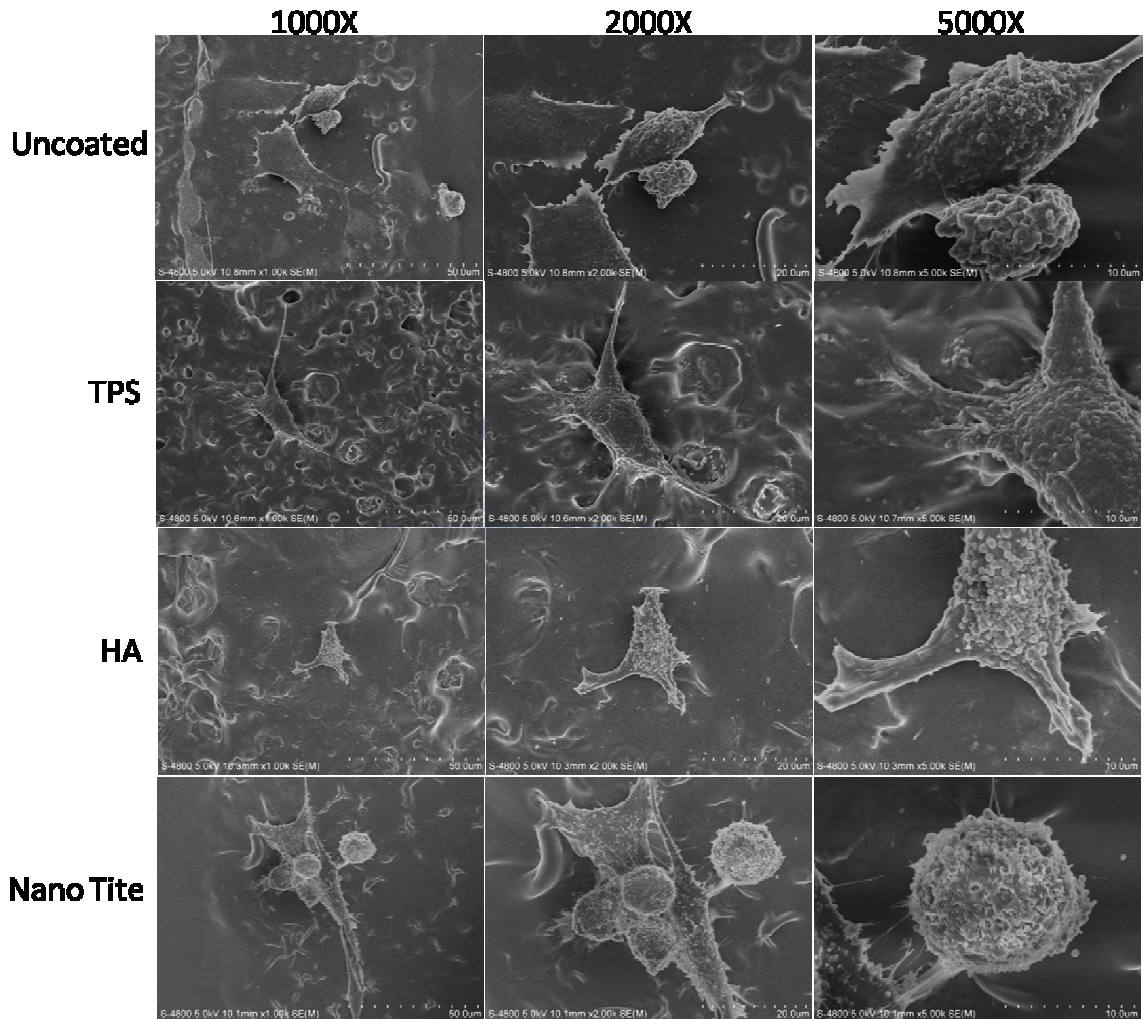


Fig. 9 SEM image for MG63 grown onto implants. Cells are grown onto implants for 7 days and harvest. The morphology of cells indicated healthy growth for HA and TPS. Cell morphology shown in Uncoated and Nano Tite indicated apoptotic growth.

1.3.6 Clinical outcomes

During a 2-year period (2007–2008), 44 patients (18 male, 26 female) aged between 33 and 82 years (mean 55) received dental implantation using Uncoated, TPS, HA, and Nano Tite. The time for stabilization of implants was recorded (Table 2). Among all patients, 7 patients received multiple types of implants (Table 3).

Table 2 clinical outcome for dental implants

Type		Recovery Average \pm SE (day)	Number of implants
Uncoated	Smoke	97.5	1
	Nonsmoke	162.5 \pm 48.86	6
TPS	Smoke	101.25 \pm 19.12	8
	Nonsmoke	132.75 \pm 21.04	10
HA	Smoke	101.79 \pm 23.02	7
	Nonsmoke	108.46 \pm 16.70	13
NanoTite	Smoke	239.25 \pm 33.36	10
	Nonsmoke	133.93 \pm 12.93	40

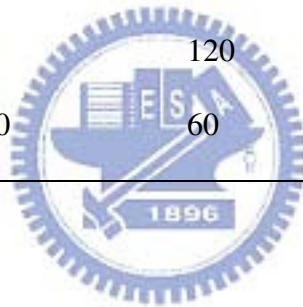
For the smoking group, HA and TPS exhibited shorter duration for the implant to stabilize in bone: 101.79 \pm 23.02 days for HA and 101.25 \pm 19.12 days for TPS. For nonsmoking group HA behaved the best with 108.46 \pm 16.70 days.

Comparison of implants within the same patient may reveal interesting result (Table 3). In general, HA is always the best with duration of stability significantly shorter among all implants. On the contrary, Nano Tite always took longest time, while TPS is between HA and Nano Tite. The clinical outcome is consistent with our in vitro evidence that HA, with

optimized nanostructure, modulates growth of osteoblast and behaves much stable than others. Nano Tite, on the contrary has less nanostructure and behaves poorly for both in vitro and clinical test.

Table 3 Clinical outcome for multiple types of implant in the same patient

Patient identity	Uncoated	TPS	HA	Nano Tite
1 (Smoker)	97.5	97.5		97.5
2 (Smoker)		60	60	360
3 (Smoker)		120	210	255
4 (Smoker)		165	82.5	270
5 (Nonsmoker)		120	90	180
6 (Nonsmoker)		120	75	300
7 (Nonsmoker)	360	60	90	



1.4 Conclusions

MG63 was grown on nanodot arrays with various sizes in diameter from 10-nm to 200-nm. Cell proliferation, morphology, adhesion, cytoskeleton, and mineralization were evaluated. Nanodot with 50-nm in diameter behaved the best in all evaluation. Four different types of dental implants were subjected for clinical test. Here we show that nanostructure is capable of modulating the in vitro growth of osteoblasts at approximately 50-nm in diameter. Best clinical outcome for dental implants with nanostructure of similar dimension behaves the best compared to nanoscaled structure (Uncoated and TPS) and undefined structure (Nano Tite).



Reference

- [1] Esposito M, Grusovin MG, Chew YS, Coulthard P, Worthington HV. Interventions for replacing missing teeth: 1- versus 2-stage implant placement. *Cochrane Database Syst Rev* 2009(3):CD006698.
- [2] Munoz-Casado MJ, Romance AI, Garcia-Recuero JI. Bioabsorbable osteofixation devices in craniosynostosis. Clinical experience in 216 cases. *Neurocirugia (Astur)* 2009 Jun;20(3):255-261.
- [3] Prowse SJ, Hold PM, Gilmour RF, Pratap U, Mah E, Kimble FW. Orbital floor reconstruction: A case for silicone. A 12 year experience. *J Plast Reconstr Aesthet Surg* 2009 Jul 9.
- [4] Toljanic JA, Baer RA, Ekstrand K, Thor A. Implant rehabilitation of the atrophic edentulous maxilla including immediate fixed provisional restoration without the use of bone grafting: a review of 1-year outcome data from a long-term prospective clinical trial. *Int J Oral Maxillofac Implants* 2009 May-Jun;24(3):518-526.
- [5] Patel S, Kurpinski K, Quigley R, Gao H, Hsiao BS, Poo MM, et al. Bioactive nanofibers: synergistic effects of nanotopography and chemical signaling on cell guidance. *Nano Lett* 2007 Jul;7(7):2122-2128.
- [6] Choi CH, Hagvall SH, Wu BM, Dunn JC, Beygui RE, CJ CJK. Cell interaction with three-dimensional sharp-tip nanotopography. *Biomaterials* 2007 Mar;28(9):1672-1679.
- [7] Park J, Bauer S, von der Mark K, Schmuki P. Nanosize and vitality: TiO₂ nanotube diameter directs cell fate. *Nano Lett* 2007 Jun;7(6):1686-1691.
- [8] Cooke MJ, Phillips SR, Shah DS, Athey D, Lakey JH, Przyborski SA. Enhanced cell attachment using a novel cell culture surface presenting functional domains from extracellular matrix proteins. *Cytotechnology* 2008 Feb;56(2):71-79.
- [9] Fine E, Zhang L, Fenniri H, Webster TJ. Enhanced endothelial cell functions on rosette nanotube-coated titanium vascular stents. *Int J Nanomedicine* 2009;4:91-97.
- [10] Harrington DA, Cheng EY, Guler MO, Lee LK, Donovan JL, Claussen RC, et al. Branched peptide-amphiphiles as self-assembling coatings for tissue engineering scaffolds. *J Biomed Mater Res A* 2006 Jul;78(1):157-167.
- [11] Kim A, Matthew Petroll W. Microtubule regulation of corneal fibroblast morphology and mechanical activity in 3-D culture. *Exp Eye Res* 2007 Oct;85(4):546-556.

- [12] McCurdy S, Baicu CF, Heymans S, Bradshaw AD. Cardiac extracellular matrix remodeling: Fibrillar collagens and Secreted Protein Acidic and Rich in Cysteine (SPARC). *J Mol Cell Cardiol* 2009 Jul 3.
- [13] Schlunck G, Han H, Wecker T, Kampik D, Meyer-ter-Vehn T, Grehn F. Substrate rigidity modulates cell matrix interactions and protein expression in human trabecular meshwork cells. *Invest Ophthalmol Vis Sci* 2008 Jan;49(1):262-269.
- [14] Kim DH, Han K, Gupta K, Kwon KW, Suh KY, Levchenko A. Mechanosensitivity of fibroblast cell shape and movement to anisotropic substratum topography gradients. *Biomaterials* 2009 Jul 10.
- [15] Tsai WB, Lin JH. Modulation of morphology and functions of human hepatoblastoma cells by nano-grooved substrata. *Acta Biomater* 2009 Jun;5(5):1442-1454.
- [16] Bruckmann C, Walboomers XF, Matsuzaka K, Jansen JA. Periodontal ligament and gingival fibroblast adhesion to dentin-like textured surfaces. *Biomaterials* 2005 Jan;26(3):339-346.
- [17] Hsin YL, Hwang KC, Yeh CT. Poly(vinylpyrrolidone)-modified graphite carbon nanofibers as promising supports for PtRu catalysts in direct methanol fuel cells. *J Am Chem Soc* 2007 Aug 15;129(32):9999-10010.
- [18] Li XT, Zhang Y, Chen GQ. Nanofibrous polyhydroxyalkanoate matrices as cell growth supporting materials. *Biomaterials* 2008 Sep;29(27):3720-3728.
- [19] Ahmed I, Liu HY, Mamiya PC, Ponery AS, Babu AN, Weik T, et al. Three-dimensional nanofibrillar surfaces covalently modified with tenascin-C-derived peptides enhance neuronal growth in vitro. *J Biomed Mater Res A* 2006 Mar 15;76(4):851-860.
- [20] Lim JY, Hansen JC, Siedlecki CA, Runt J, Donahue HJ. Human foetal osteoblastic cell response to polymer-demixed nanotopographic interfaces. *J R Soc Interface* 2005 Mar 22;2(2):97-108.

Chapter II

2.1 Introduction

The development of invasive and metastatic cancer cells is complicated [1-4]. Invasion of cancer cells begins by breaking away from primary tumor and crawling through surrounding tissue, followed by moving into circulation and transported through the body, and establishing a secondary tumor. Changes in motility and the production of enzymes that will break through surrounding tissue are characteristic to invasive cancer cells. Genes such as KCl cotransporter family (KCC) [5, 6] and actinin-4 [7-10], are associated with invasive ability of cancer cells. KCl cotransport plays a crucial role in the growth and invasion of human cervical cancer. Actinin-4 is a biomarker of cancer invasion and an indicator of prognosis for cancer patients. A fast and convenient platform might be beneficial in obtaining additional factors and parameters that control or manipulate invasive properties of cancer cells.

Finding the optimized surface for cells to grow is very important in tissue engineering. Many researchers have modulated of cell growth and apoptosis by using different material to fabricate the surface, coating extracellular matrix (ECM), or growth factor in recent years [11-25]. Many studies indicate that nanostructure such as nanofiber, sharp-tip, or nanotube affect cell proliferation. Nanofiber could guide the dimension of cell proliferation [11]. As the nanotopographical three-dimensionality of sharp-tip increased, the consistent trend of fewer cells and smaller cell size was observed [13]. Cell adhesion and spreading were severely impaired on nanotube layers with a tube diameter larger than 50-nm, resulting in dramatically reduced cellular activity and a high extent of programmed cell death [15]. In our previous studies, we have shown differential growth of NIH-3T3 cells onto nanodot arrays with dot

diameters ranging from 10-nm to 200-nm. Cells grew normally on the 10-nm array and on flat surfaces. However, 50-nm, 100-nm, and 200-nm nanodot arrays induced apoptotic events. The occurrence of apoptosis is mediated by the formation of focal adhesions. Application of assembly containing a range of nanostructures should be capable of obtaining parameters that are useful in the designing and evaluation of artificial implants in tissue engineering.

In the current study, we have fabricated a nanodevice consisting a matrix of 9 nanodot arrays with various dot size ranging from flat surface to 200-nm. We applied this device to survey the basic parameters of cancer cell lines. Apparently, the device was capable of distinguishing cancer cell line of various stages and also provided basic designing parameters for artificial implants. Our device will serve as a convenient and fast tool for tissue engineering and cancer treatment.



2.2 Experimental Methods

2.2.1 Chemicals

Glutaraldehyde and osmium tetroxide were purchased from Electron Microscopy Sciences (USA). Anti-vinculin mouse antibody was purchased from Abcam (USA). Alexa Fluor 594 phalloidin, and Alexa Fluor 488 goat anti-mouse IgG were purchased from Invitrogen (USA). Trypsin was purchased from Sigma (USA). Polydimethylsiloxane (PDMS) was purchased from Sil-More (Taiwan). Other chemicals of analytical grade or higher were purchased from Sigma or Merck.

2.2.2 Fabrication of the nanodevice, a matrix of nanodot arrays

Nanodot arrays were fabricated as described [26]. Tantalum nitride (TaN) thin film of 200-nm in thickness was deposited onto a 6-inch silicon wafer followed by deposition of 400nm-thick aluminum on the top of a TaN layer. Anodization was carried out in 1.8 M sulfuric acid at 5 Volts for 10-nm nanodot array, in 0.3 M oxalic acid at 25 Volts, and 100 Volts for 50-nm, and 100-nm nanodot arrays or in 5 % (w/v) Phosphate acid (H_3PO_4) at 100 Volts for 200-nm nanodot arrays, respectively. Porous anodic alumina was formed during the anodic oxidation. The underlying TaN layer was oxidized into tantalum oxide nanodots using the alumina nanopores as template. The porous alumina was removed by immersing in 5 % (w/v) H_3PO_4 overnight. A thin layer of platinum (ca 5-nm) was sputtered onto the structure to improve biocompatibility. The dimension and homogeneity of nanodot arrays were measured and calculated from images taken by JEOL JSM-6500 TFE-Scanning electron microscopy (SEM).

The fabricated nanodot arrays were cut into 1 cm x 1 cm squares and integrated into a 3

by 3 matrix set of PDMS frame (Fig. 1c). The PDMS frame was molded by a glass template which was fabricated by photolithography [27]. Before curing, the template covered PDMS was placed for 1 hour to let all bubbles in the PDMS layer escaped. The curing was performed by heating the PDMS up to 75°C in an oven for about 45 minutes. The final matrix contains a flat surfaced square at the center with surrounding nanodot arrays ranging from 10-nm to 200-nm (Fig. 1c).

2.2.3 Cell culture

Cell lines were summarized in Table 1. HELA, PA-1, MG63 cells were cultured in Dulbecco's Modified Eagle's Medium (DMEM) complimented with 10% fetal bovine serum (FBS) and 5% CO₂ and incubated at 37 °C. ES2 cells were cultured in DMEM complimented with 10% fetal calf serum (FCS) and 5% CO₂ and incubated at 37 °C. C33A cells were cultured in MEM Alpha complimented with 10% FBS and 5% CO₂ and incubated at 37 °C. TOV-112D, and TOV-21G cells were cultured in MCDB105 and Medium199 complimented with 15% FBS and 5% CO₂ and incubated at 37 °C.

2.2.4 Scanning electron microscopy

The harvested cells were fixed with 1% glutaraldehyde in phosphate buffered saline (PBS) at 4 °C for 20 minutes, followed by post-fixation in 1% osmium tetroxide for 30 minutes. Dehydration was performed through a series of ethanol concentrations (5 minutes incubation each in 50%, 60%, 70%, 80%, 90%, 95%, and 100% ethanol) and air dried. The specimen was sputter-coated with platinum and examined by JEOL JSM-6500 TFE-SEM at an accelerating voltage of 10 keV. We randomly picked five SEM pictures for each condition and calculated the number of abnormal cells and the amount of cells.

2.2.5 Immunostaining of vinculin and actin filament

Cells were harvested and fixed with 4% paraformaldehyde in PBS for 15 minutes followed by PBS wash for three times. Membrane was permeated by incubating in 0.1 % Triton X-100 for 10 minutes, followed by PBS wash for three times, blocked by 1 % bovine serum albumin (BSA) in PBS for 1 hour, and PBS wash for three times. The sample was incubated with anti-vinculin antibody (properly diluted in 0.5 % BSA) and phalloidin for 1 hour, followed by incubating with Alexa Fluor 488 goat anti-mouse antibody for 1 hour followed by PBS wash for three times. We randomly picked five fluorescent pictures for each condition and calculated the number of focal adhesions (i.e. green spots of vinculin) per cell.

2.2.6 Definition for the scores of proliferation, apoptosis, focal adhesion, and cytoskeleton organization

“P” represents proliferation score. “P” is calculated from the cell density relative to cell density on flat surface. “P” of flat surface is 100%. “A” represents apoptosis score. “A” is the percentage of apoptotic cells in a culture. “F” represents adhesion score. “F” is calculated from number of focal adhesions per cell and compared to number of focal adhesions on flat surface. “C” represents cytoskeleton organization score. “C” is calculated from dividing the number of actin filament per cell by the number of actin filament for cells grown on flat surface.

2.3 Results and Discussions

2.3.1 The fabrication of an integrated nanodot array device

The 3 x 3 matrix is composed of 9 nanodot arrays with dot size ranging from 10-nm to 200-nm. Each array is cut into a 1cm x 1cm square and assembled as a matrix by fitting into a preformed PDMS frame.

Nanodot arrays were fabricated by AAO processing on tantalum-coated wafer [26]. Tantalum oxide nanodot arrays with dot diameters of 10-nm, 50-nm, 100-nm, and 200-nm were constructed by different solution and voltage on silicon wafer (Fig. 1a). To provide a biocompatible and unique interacting surface, platinum of ca 5-nm thickness was sputter-coated onto the top of the nanodot. SEM showed diameters of 10 ± 2.8 nm, 52 ± 5.6 nm, 102 ± 9.2 nm, and 212 ± 18.6 nm for 10-nm, 50-nm, 100-nm, and 200 nm dot arrays, respectively (Fig. 1b). Dimensions of nanodots were well-controlled and highly defined.

The fabricated nanodot arrays were cut into 1cm x 1 cm squares and integrated into a 3 x 3 matrix set on PDMS frame (Fig. 1c). The PDMS frame was molded by a glass template which was fabricated by photolithography [27]. The final matrix contains a flat surfaced square at the center with surrounding nanodot arrays ranging from 10-nm to 200-nm (Fig. 1c).

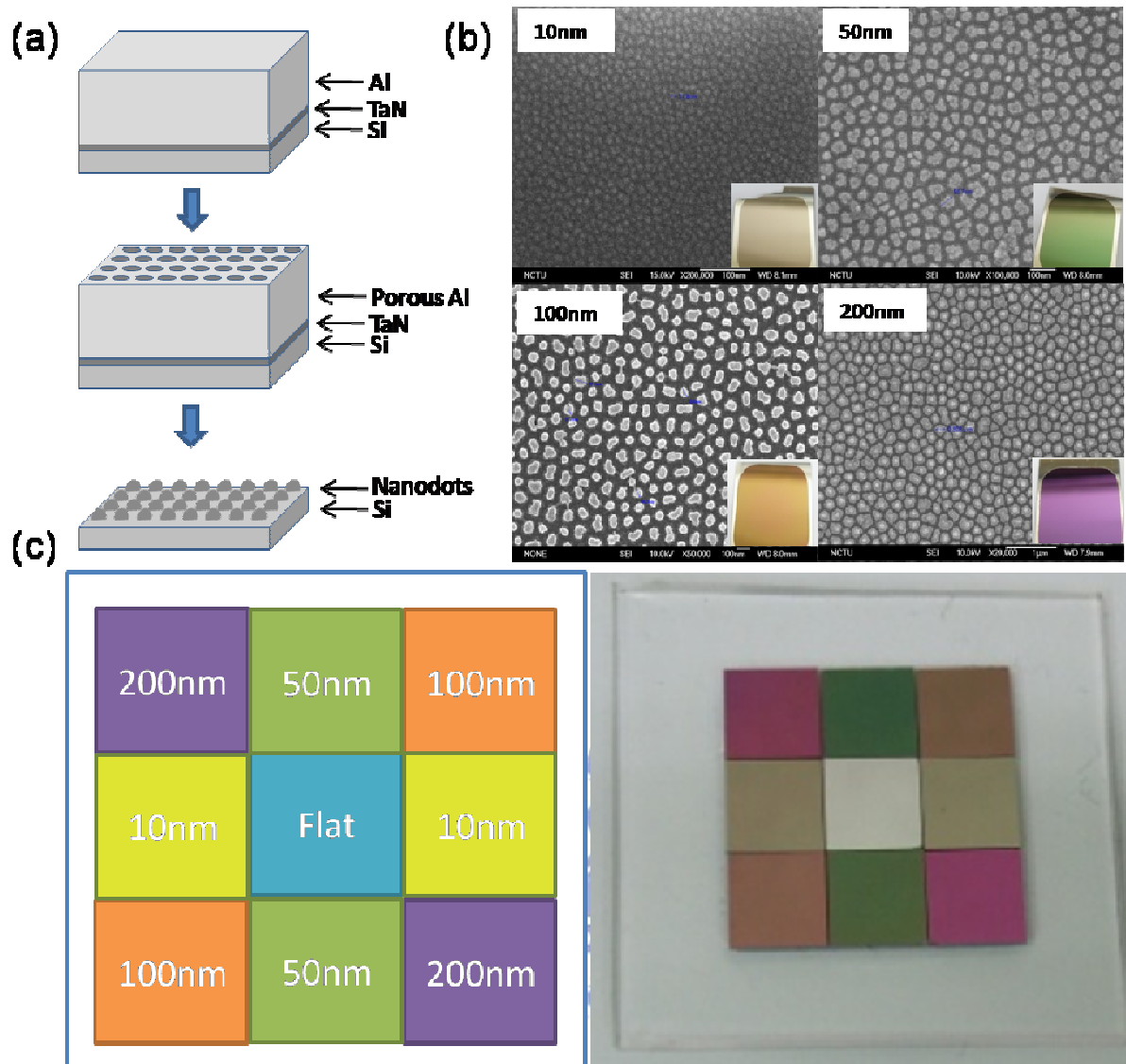


Fig. 1. Fabrication of integrated nanodevice for the screening of cellular response. (A) Schematic representation for the fabrication of tantalum-based nanodot arrays using AAO processing. (B) SEM images of the tantalum oxide nanodot arrays with dot diameters of 10-nm, 50-nm, 100-nm, and 200-nm were constructed on silicon wafer. (C) Schematic drawing of integrated nanodevice (left) and photograph (right).

2.3.2 Assessment of proliferation, apoptosis, cell adhesion, and cytoskeleton reorganization for cultured cells

To define parameters that modulate the proliferation and apoptosis of cells and to assess the cellular response against varied nanostructured surface, the integrated nanodevice was placed in the culture dish. HELA, C33A, ES2, PA-1, TOV-112D, TOV-21G, MG63, and NIH-3T3 cells were seeded on the device and cultured for 3 day (Table 1). Among them NIH-3T3 cells were incorporated as control cell line for normal fibroblasts. Cell density was counted to examine the proliferation of cells. SEM was performed to assess the morphological change of cells (Fig. 2). To evaluate cell adhesion and cytoskeleton reorganization, immunostaining specific to vinculin and actin filaments was performed (Fig. 3 and Fig. 4). The scores of cell proliferation, morphology, distribution of focal adhesions, and cytoskeleton organization were summarized in Table 2.

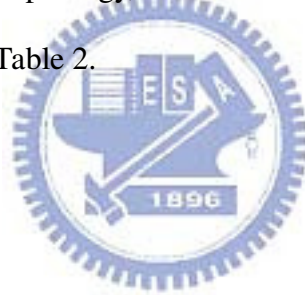


Table 1. cell lines tested by the nanotopography

Cancer type	Name	Cell type	Clinical origin	Description
Cervical carcinoma	HELA	Epithelial	adenocarcinoma	Low p53 expression, contain HPV-18
	C33A	Epithelial	carcinoma	Negative for HPV DNA and RNA
Ovarian carcinoma	ES2	Fibroblast	Clear cell carcinoma	Low P glycoprotein expression
	PA-1	Epithelial	teratocarcinoma	Have diploid female karyotype with a translocation between chromosomes 15 and 20.
	TOV-112D	Epithelial	adenocarcinoma	Grade 3, stage III
	TOV-21G	Epithelial	Clear cell carcinoma	Grade 3, stage III
Osteosarcoma	MG63	Osteoblast	osteosarcoma	Produce high yields of interferon after superinduction with polyinosinic acid, polycytidylic acid, cycloheximide and actinomycin D
	NIH-3T3	Fibroblast		Highly contact inhibited and sensitive to sarcoma virus focus formation and leukaemia virus propagation

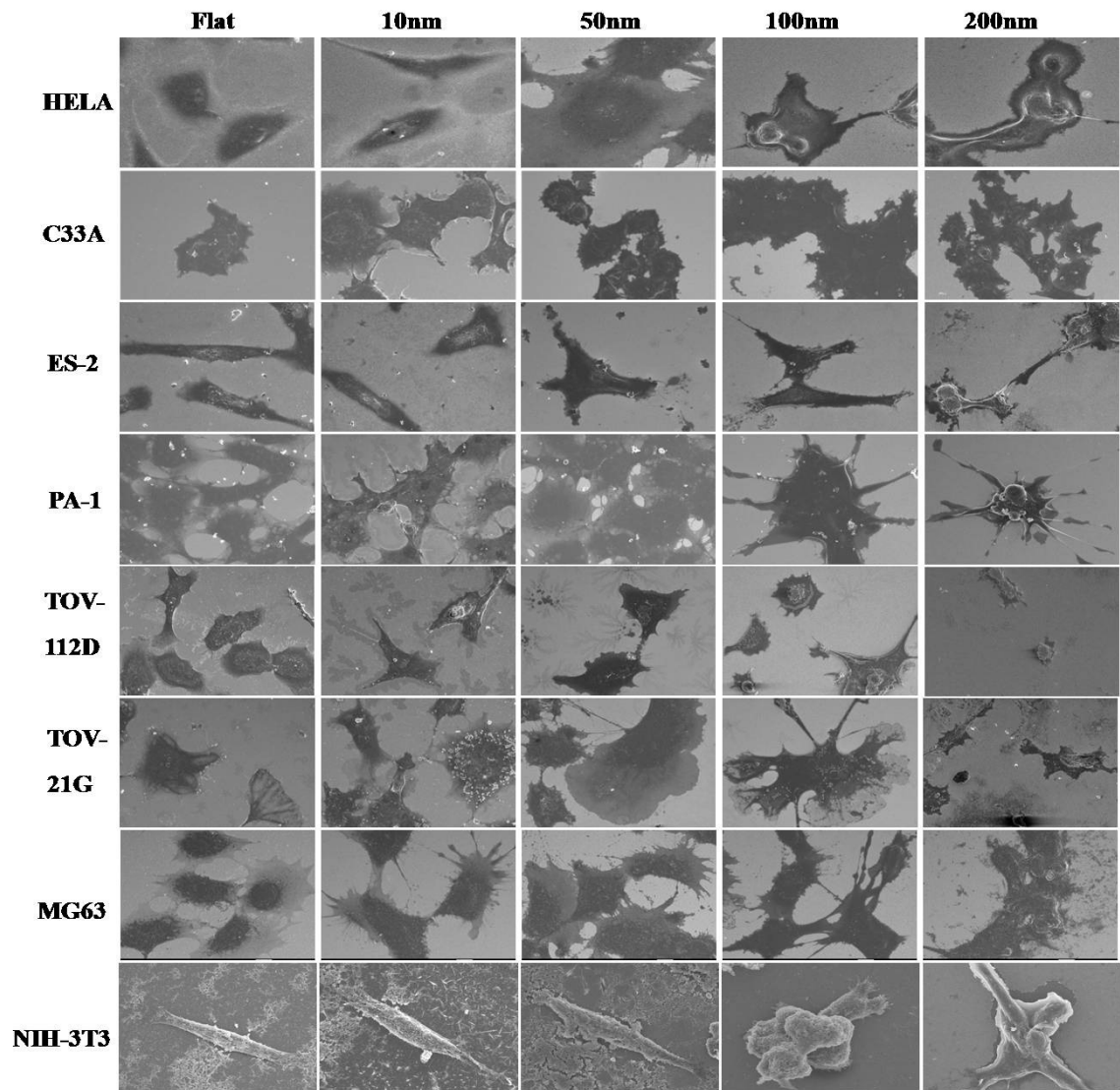


Fig. 2. SEM images of cells seeded on nanodot arrays. HELA, C33A, ES-2, PA-1, TOV-112D, TOV-21G, MG63, and NIH-3T3 cells were seeded on flat silicon surface, 10-nm nanodot array (10-nm), 50-nm nanodot array (50-nm), 100-nm nanodot array (100-nm), and 200-nm nanodot array (200-nm). The cells were harvested at 72 hours (Day 3) after seeding. SEM images were taken. Representative images are shown.

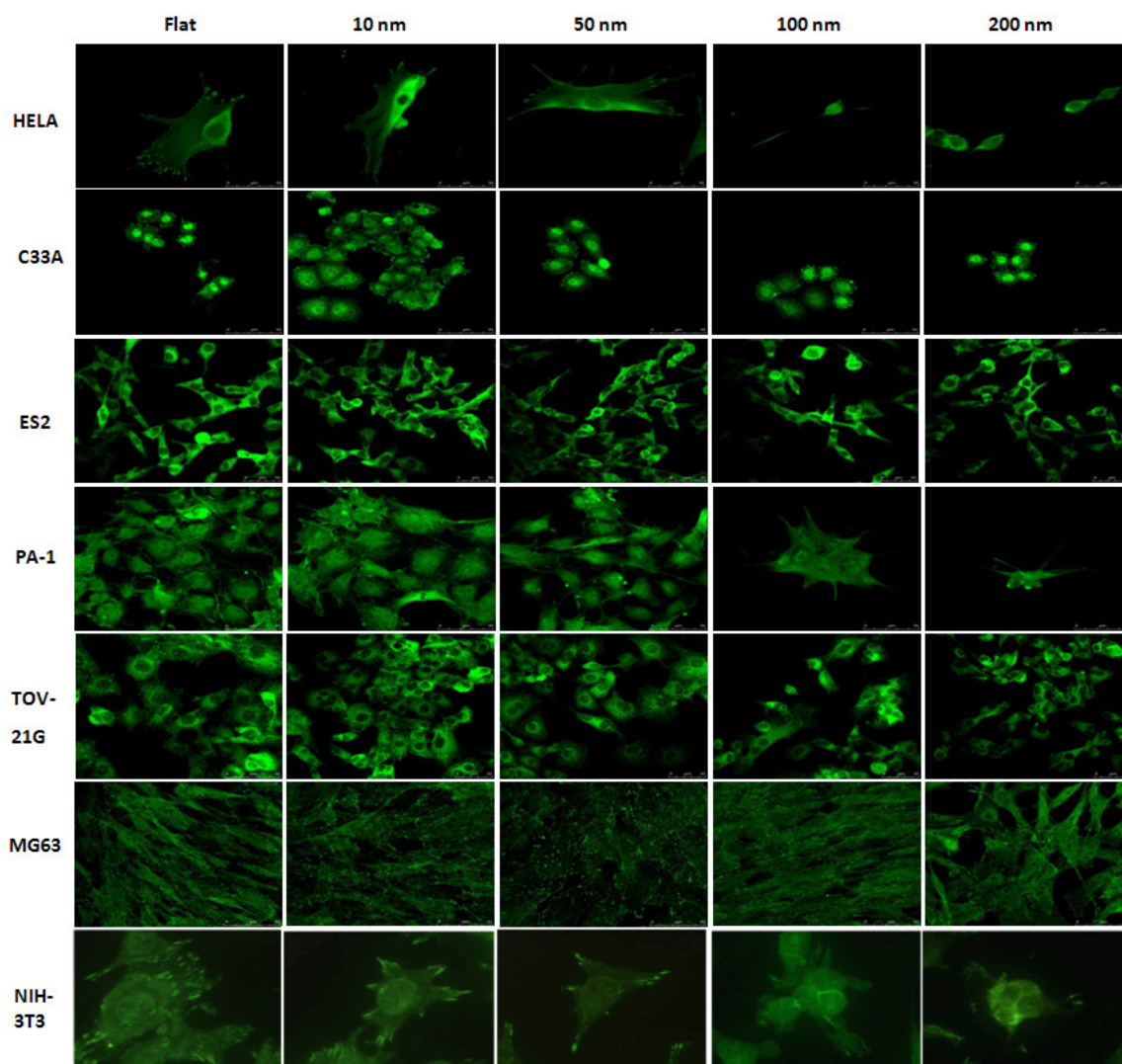


Fig. 3. Immunostaining to show distribution of vinculin in cell cultured on 10-nm, 50-nm, 100-nm, and 200-nm nanodot arrays and on flat surface. Cells were seeded on the arrays for 72 hours before harvest. The sample was incubated with anti-vinculin antibody (properly diluted in 0.5 % BSA), followed by incubating with Alexa Fluor 488 goat anti-mouse antibody.

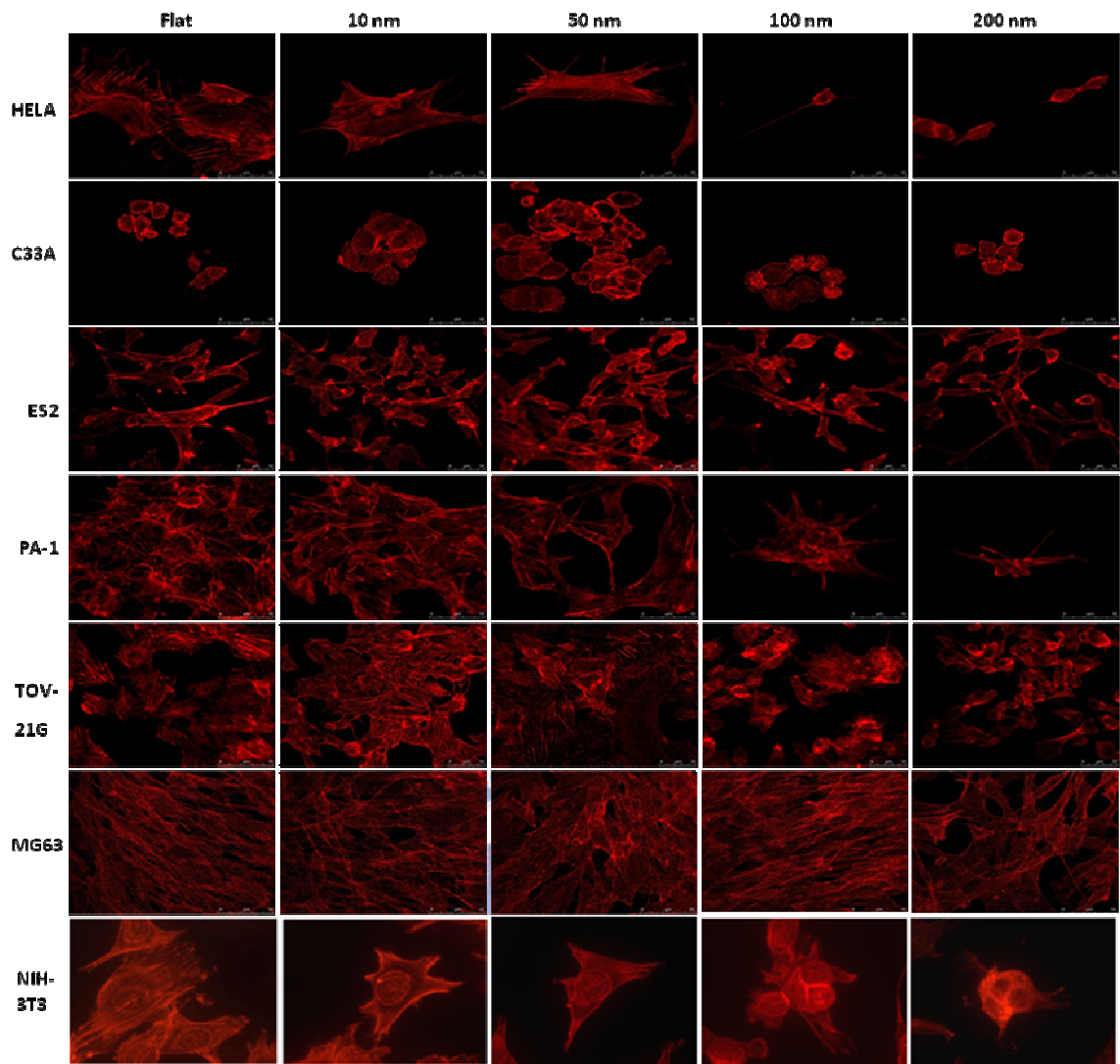


Fig. 4. Immunostaining to show distribution of actin filament in cell cultured on 10-nm, 50-nm, 100-nm, and 200-nm nanodot arrays and on flat surface. Cells were seeded on the arrays for 72 hours before harvest. The sample was incubated with phalloidin.

HELA cells are a human cervical cancer cell line carrying human papillomavirus-18 (HPV-18), with a low level of p53 expression. It is an immortal cell line used in scientific research. Proliferation was enhanced and reached to maximum at 50-nm, but dropped dramatically to 60% when the size reached to 100-nm, and to 20% for 200-nm nanodot array. The morphology remained flat and extended at 50-nm, but mounted and changed to apoptosis-like shape for 100-nm and 200-nm surface. The immunostaining indicated

enhanced staining of vinculin which represents enhanced cell adhesion for size under 50-nm. The cytoskeleton organization loses its order when the size bigger than 100-nm. In summary, HELA cell grew well and reached optimized condition at 50-nm, but lost cell adhesion and switched to apoptosis when the dot size is bigger than 100-nm.

C33A cell is a human cervical cancer cell line. It is derived from advanced carcinoma with highly invasive activity and with negative express for HPV DNA and RNA. No significant difference of proliferation among all nanodot arrays, from flat to 200-nm, was observed. The cell morphology remained flat and extended at all sizes of the nanodot arrays. The immunostaining showed no significant difference in the number of focal adhesions. Cells grown at all conditions showed well organized cytoskeleton. In summary, C33A cells grew well on all sizes of the nanodot arrays.

The ES-2 cell line was established from a surgical tumor specimen taken from a 47-year-old black woman. The tumor was described as a poorly differentiated ovarian clear cell carcinoma. It exhibits low to moderate resistance to a number of chemotherapeutic agents including doxorubicin, cisplatin, carmustine, etoposide and cyanomorpholinodoxorubicin (MRA-CN). It also expresses low levels of P glycoprotein. The proliferation for ES2 dropped to 80% at 100-nm and to 60% for 200-nm. The morphology was extended from flat surface to 100-nm nanodots. The morphology indicated apoptosis occurred when the size reached 200-nm. The immunostaining of vinculin shows that the number of focal adhesions decreased dramatically when grow on 200-nm dot array. Cytoskeleton organization became disordered at 200-nm. In summary, ES2 cell grows well from flat to 100-nm but dropped to apoptosis and lost cell adhesion at 200-nm.

The human ovarian teratocarcinoma cell line PA-1 was isolated from the ascites fluid of a 12-year-old girl suffering from recurrent malignant teratocarcinoma. Malignant ovarian teratocarcinomas differ from their benign counterparts in that they are a rare form of tumor

and usually occur in prepubertal females. They consist of many immature elements and can arise by several mechanisms including failure of meiosis I or II or fusion of two ova. High passage PA-1 cells are tumorigenic in nude mice upon s.c. injection, form embryoid bodies under nonadherent culture conditions, and form colonies in soft agar. Cytogenetically, PA-1 has a stable diploid female karyotype with a single, balanced translocation between chromosomes 15 and 20. Proliferation was enhanced and rises to 120% at 50-nm, but decreased to 40% when the size reached 100-nm and to 10% at 200-nm. The morphology remained flat and extended until 50-nm, but mounted and started apoptosis from 100-nm and 200-nm. Decreased staining of vinculin was observed which indicated decreased cell adhesion for size bigger than 100-nm. The cytoskeleton organization was less ordered when the size was bigger than 100-nm. In summary, PA-1 cell grows well and reached to the optimized condition at 50-nm, but dropped to apoptosis and loses cell adhesion if the size is bigger than 100-nm.

TOV-112D cells are a human ovarian cancer cell line. These cells are from an endometrioid epithelial carcinoma derived from 42-year-old female. It is a primary malignant adenocarcinoma with grade 3 and staged IIIC. Proliferation did not change from flat to 50-nm, but decreased to 70% when the size was 100-nm and to 50% at 200-nm. The morphology remained flat and extended at 50-nm, but mounted and apoptosis at 100-nm and 200-nm dot arrays. In summary, TOV-112D cell grows well on flat, 10-nm, and 50-nm surface, but dropped to apoptosis if the size is bigger than 100-nm.

TOV-21G cells are a human ovarian cancer cell line. These cells are from a clear cell epithelial carcinoma derived from 62-year-old female. It is a primary malignant adenocarcinoma with grade 3 and staged III. Proliferation was enhanced and reached to 110% at 50-nm, but decreased to 90% when the size was 100-nm and to 60% at 200-nm. The morphology remained flat and extended at 50-nm, but mounted and apoptosis at 100-nm and

200-nm dot arrays. The immunostaining indicated a little enhance staining of vinculin for size under 50-nm. The cytoskeleton organization loses its order when the size bigger than 100-nm. In summary, TOV-21G cell grows well on flat, 10-nm, and 50-nm surface, but dropped to apoptosis and loses cell adhesion if the size is bigger than 100-nm.

MG-63 cells, a cell line derived from an osteosarcoma, produce high yields of interferon after superinduction with polyinosinic acid, polycytidylic acid, cycloheximide and actinomycin D. Studies using MG-63 cells provide some important mechanistic clues concerning the details of the amplification process in tumors. Proliferation was enhanced and reached to 120% at 50-nm, but dropped to 90% at 100-nm, and to 70% for 200-nm nanodot array. The morphology became more flat and extended at 50-nm, but mounted and changed to apoptosis shape for 100-nm and 200-nm dots array surface. The immunostaining showed enhanced staining of vinculin which represents enhanced cell adhesion for size under 50-nm. The cytoskeleton organization loses its order when the size bigger than 100-nm. In summary, MG63 cell grows well and reach to the optimized condition at 50-nm, but dropped to apoptosis and loses cell adhesion if the size is bigger than 100-nm.

NIH-3T3 cell is a mouse embryonic fibroblast cell line. These cells are established from a NIH Swiss mouse embryo. They are highly contact inhibited and are sensitive to sarcoma virus focus formation and leukaemia virus propagation. This cell line was established from NIH Swiss mouse embryo cultures in the same manner as the original random bred 3T3 and the inbred BALB/c 3T3. The established NIH-3T3 line was subjected to more than 5 serial cycles of subcloning in order to develop a subclone with morphologic characteristics best suited for transformation assays. It is therefore used for DNA transinfection studies. Proliferation was normalized at flat, 10-nm, and 50-nm dot arrays, but dropped to 70% at 100-nm, and to 50% for 200-nm nanodot arrays. The morphology mounted and changed to apoptosis shape for 100-nm and 200-nm dots array surface. The immunostaining indicated no

difference for size between flat and 50-nm. The cytoskeleton organization loses its order when the size bigger than 100-nm. In summary, NIH-3T3 cell grows well on flat, 10-nm, and 50-nm, but dropped to apoptosis and loses cell adhesion if the size is bigger than 100-nm.

There are two cervical cancer cell lines screened, HELA cell and C33A. C33A represents a late-staged and advanced cancer while HELA cell is less malignant in clinical stages. The indexes of proliferation, apoptosis, adhesion, and cytoskeleton were consistent with the staged index and also with the in vivo invasive ability of cancer cells. The proliferation of HELA cells dropped, appeared apoptosis, and lost cell adhesion if the size was bigger than 100-nm. But the nanodot arrays did not affect the proliferation of C33A cells. C33A cells had more resistant to the nanostructure than HELA cells. The nanodevice is capable of judging the clinical stage and invasive ability of cancer cells.

There were 4 ovarian cancer cell lines tested. There are clear cell carcinoma (ES2, TOV-21G), endometriod carcinoma (TOV-112D), and teratocarcinoma (PA-1). There are grad 3/stage III carcinomas (TOV-112D and TOV-21G). The results showed that PA-1 and TOV-112D grew poorly if the size was bigger than 100-nm, but the nanostructure was not seriously influence for ES2 and TOV-21G cells. For ovarian cancer, the indexes of proliferation, apoptosis, adhesion, and cytoskeleton were also consistent with the staged index and with the in vivo invasive ability of cancer cells. Although TOV-21G and TOV-112D are in the same grade, TOV-21G has stronger invasive ability than TOV-112D. The nanodevice is capable of judging the stage and the invasive ability of two cells.

Parameters for the Control of cell growth can be derived instantly from our nanodevice. For dental implants, the biocompatibility between implants and osteoblasts determines the success of operation and long term maintenance. The parameters derived from the current study can provide pivotal information in designing and fabrication for the dental implant. In other cases, implants such as cardiovascular stent, also requires the accurate control for the

growth of epithelial cells and smooth muscle cells. The surface in contact with these live tissues can be designed to match the expected performance of the stents.

Table 2. Scores of cell proliferation (cell density), apoptosis (cell bulge), focal adhesion (vinculin number), and cytoskeleton (F-actin organization) for cells grown on the nanodevice.

Cell line	Flat				10 nm				50 nm				100 nm				200 nm			
	P ^a (%)	A ^b (%)	F ^c (%)	C ^d (%)	P(%)	A(%)	F(%)	C(%)	P(%)	A(%)	F(%)	C(%)	P(%)	A(%)	F(%)	C(%)	P(%)	A(%)	F(%)	C(%)
HELA	100	0	100	100	110	0	110	110	120	0	120	120	60	50	60	40	20	80	20	20
C33A	100	0	100	100	100	0	100	100	100	0	100	100	100	0	100	100	100	0	100	100
ES2	100	0	100	100	100	0	100	100	100	0	100	100	80	10	80	80	60	50	60	60
PA-1	100	0	100	100	110	0	100	100	120	0	100	100	40	50	40	60	10	100	10	10
TOV-112D	100	0			100	0			100	0			70	50			50	80		
TOV-21G	100	0	100	100	100	0	100	100	110	0	110	110	90	10	80	80	60	40	60	60
MG63	100	0	100	100	110	0	110	110	120	0	120	120	90	20	90	90	70	40	60	70
NIH-3T3	100	0	100	100	100	0	90	90	100	0	80	80	70	60	40	40	50	90	20	20

^a“P” elicits proliferation score. “P” is calculated from the cell density and expressed in percentage. Cell density on flat surface is 100%.

^b“A” elicits apoptosis score. “A” is the percentage of apoptotic cells in a culture.

^c“F” elicits adhesion score. “F” is calculated from number of focal adhesions per cell and compared to flat surface.

^d“C” elicits cytoskeleton organization score. “C” is calculated from dividing the number of actin filament per cell by the number of actin filament for cells grown on flat surface.

2.4 Conclusions

We have established a platform which can assess basic parameters for cell growth. The specific platform could be used to observe the proliferation, apoptosis, adhesion, and cytoskeleton organization of cells. The simplified fabrication process ensured mass production and cost down. Apparently, the device was capable of distinguishing cancer cell line of various stages and also provided basic designing parameters for artificial implants. Our device will serve as a convenient and fast tool for tissue engineering and cancer treatment.



Reference

- [1] Bacac M, Stamenkovic I. Metastatic cancer cell. *Annu Rev Pathol* 2008;3:221-247.
- [2] Friedl P, Wolf K. Tumour-cell invasion and migration: diversity and escape mechanisms. *Nat Rev Cancer* 2003 May;3(5):362-374.
- [3] Reuning U, Magdolen V, Wilhelm O, Fischer K, Lutz V, Graeff H, et al. Multifunctional potential of the plasminogen activation system in tumor invasion and metastasis (review). *Int J Oncol* 1998 Nov;13(5):893-906.
- [4] Stetler-Stevenson WG, Aznavoorian S, Liotta LA. Tumor cell interactions with the extracellular matrix during invasion and metastasis. *Annu Rev Cell Biol* 1993;9:541-573.
- [5] Shen MR, Chou CY, Hsu KF, Hsu YM, Chiu WT, Tang MJ, et al. KCl cotransport is an important modulator of human cervical cancer growth and invasion. *J Biol Chem* 2003 Oct 10;278(41):39941-39950.
- [6] Shen MR, Chou CY, Ellory JC. Volume-sensitive KCl cotransport associated with human cervical carcinogenesis. *Pflugers Arch* 2000 Sep;440(5):751-760.
- [7] Yamamoto S, Tsuda H, Honda K, Kita T, Takano M, Tamai S, et al. Actinin-4 expression in ovarian cancer: a novel prognostic indicator independent of clinical stage and histological type. *Mod Pathol* 2007 Dec;20(12):1278-1285.
- [8] Honda K, Yamada T, Hayashida Y, Idogawa M, Sato S, Hasegawa F, et al. Actinin-4 increases cell motility and promotes lymph node metastasis of colorectal cancer. *Gastroenterology* 2005 Jan;128(1):51-62.
- [9] Honda K, Yamada T, Endo R, Ino Y, Gotoh M, Tsuda H, et al. Actinin-4, a novel actin-bundling protein associated with cell motility and cancer invasion. *J Cell Biol* 1998 Mar 23;140(6):1383-1393.
- [10] Yamagata N, Shyr Y, Yanagisawa K, Edgerton M, Dang TP, Gonzalez A, et al. A training-testing approach to the molecular classification of resected non-small cell lung cancer. *Clin Cancer Res* 2003 Oct 15;9(13):4695-4704.
- [11] Patel S, Kurpinski K, Quigley R, Gao H, Hsiao BS, Poo MM, et al. Bioactive nanofibers: synergistic effects of nanotopography and chemical signaling on cell guidance. *Nano Lett* 2007 Jul;7(7):2122-2128.
- [12] Tan J, Saltzman WM. Biomaterials with hierarchically defined micro- and nanoscale structure. *Biomaterials* 2004 Aug;25(17):3593-3601.

- [13] Choi CH, Hagvall SH, Wu BM, Dunn JC, Beygui RE, CJ CJK. Cell interaction with three-dimensional sharp-tip nanotopography. *Biomaterials* 2007 Mar;28(9):1672-1679.
- [14] Wood MA. Colloidal lithography and current fabrication techniques producing in-plane nanotopography for biological applications. *J R Soc Interface* 2007 Feb 22;4(12):1-17.
- [15] Park J, Bauer S, von der Mark K, Schmuki P. Nanosize and vitality: TiO₂ nanotube diameter directs cell fate. *Nano Lett* 2007 Jun;7(6):1686-1691.
- [16] Rebollar E, Frischauf I, Olbrich M, Peterbauer T, Hering S, Preiner J, et al. Proliferation of aligned mammalian cells on laser-nanostructured polystyrene. *Biomaterials* 2008 Apr;29(12):1796-1806.
- [17] Cukierman E, Pankov R, Stevens DR, Yamada KM. Taking cell-matrix adhesions to the third dimension. *Sci* 2001 Nov 23;294(5547):1708-1712.
- [18] Zinger O, Anselme K, Denzer A, Habersetzer P, Wieland M, Jeanfils J, et al. Time-dependent morphology and adhesion of osteoblastic cells on titanium model surfaces featuring scale-resolved topography. *Biomaterials* 2004 Jun;25(14):2695-2711.
- [19] Harrington DA, Cheng EY, Guler MO, Lee LK, Donovan JL, Claussen RC, et al. Branched peptide-amphiphiles as self-assembling coatings for tissue engineering scaffolds. *J Biomed Mater Res A* 2006 Jul;78(1):157-167.
- [20] Cooke MJ, Phillips SR, Shah DS, Athey D, Lakey JH, Przyborski SA. Enhanced cell attachment using a novel cell culture surface presenting functional domains from extracellular matrix proteins. *Cytotechnology* 2008 Feb;56(2):71-79.
- [21] Fine E, Zhang L, Fenniri H, Webster TJ. Enhanced endothelial cell functions on rosette nanotube-coated titanium vascular stents. *Int J Nanomedicine* 2009;4:91-97.
- [22] Sharma S, Soni VP, Bellare JR. Chitosan reinforced apatite-wollastonite coating by electrophoretic deposition on titanium implants. *J Mater Sci Mater Med* 2009 Jul;20(7):1427-1436.
- [23] Avila G, Misch K, Galindo-Moreno P, Wang HL. Implant surface treatment using biomimetic agents. *Implant Dent* 2009 Feb;18(1):17-26.
- [24] Goransson A, Arvidsson A, Currie F, Franke-Stenport V, Kjellin P, Mustafa K, et al. An in vitro comparison of possibly bioactive titanium implant surfaces. *J Biomed Mater Res A* 2009 Mar 15;88(4):1037-1047.
- [25] Lim TY, Poh CK, Wang W. Poly (lactic-co-glycolic acid) as a controlled release delivery device. *J Mater Sci Mater Med* 2009 Mar 13.
- [26] Wu CT, Ko FH, Hwang HY. Self-aligned tantalum oxide nanodot arrays through anodic alumina template. *MiEng* 2006 Apr-Sep;83(4-9):1567-1570.

|

[27] Zaouk R, Park BY, Madou MJ. Fabrication of polydimethylsiloxane microfluidics using SU-8 molds. *Methods Mol Biol* 2006;321:17-2.

